Original Paper

Landslides
DOI 10.1007/s10346-022-01960-1
Received: 11 January 2022
Accepted: 18 August 2022

Weile Li · Weiwei Zhan · Huiyan Lu · Qiang Xu · Xiangjun Pei · Dong Wang · Runqiu Huang · Daqing Ge

Precursors to large rockslides visible on optical remote-sensing images and their implications for landslide early detection

Abstract Early detection of rockslides at high-elevation and well-vegetated slopes remains challenging. This study used satellite and unmanned aerial vehicle (UAV) optical remote-sensing (ORS) images to track evidence of slope deformation and examine potential geomorphological precursors of five large rockslides in China. The multi-temporal image interpretation results were combined with available pre-sliding slope displacement data derived from synthetic aperture radar (SAR) or field monitoring to study the temporal changes in geomorphological precursors accompanying slope deformation. All the surveyed landslides had cracks or scarps and rockfalls within the landslide source area before the onset of rapid sliding. These precursors can be identified in ORS images taken several years or decades before the rapid slope failure, which provides sufficient time for the landslide early detection in practice. Local topography affects the spatial locations of cracks or scarps. Rockfalls within the landslide source area tend to locate at "key blocks" where slope mass provides forces resisting sliding. The rockfall area ratio, defined as the accumulated area of rockfalls over the landslide source area, ranged from 0.33 to 0.92 before rapid slope failure. The landslides developed on anti-dip and igneous rock slopes show a more significant rise of rockfall area ratio before the slope failure than the landslides on dip slopes. Given the broad availability of ORS data, this study could shed light on the ORS-based landslide early detection and landslide kinematics study.

Keywords Rockslide · Geomorphological precursor · Optical remote sensing · Multi-temporal analysis · Landslide early detection

Introduction

Rapid failures of rock slopes, including rock slides, avalanches, and topples, are the most striking and hazardous mass movements in high mountains (Huang 2007; Huggel 2009; Nishii et al. 2013). Many catastrophic rockslides in China are characterized as high elevation and not being identified through preliminary on-site investigations (e.g., Fan et al. 2017, 2019; Zhang et al. 2018; Ouyang et al. 2019; Gong et al. 2021). Large rock slope failures are usually nested within deep-seated gravitational slope deformations (DSGSDs), which are observable over long term (≥ 100 years) and short term (< 100 years) (Pánek and Klimeš 2016). Examining DSGSD features as potential precursors to landslides could shed light on landslide early detection and landslide kinematics studies.

Different precursory geomorphological features to slope failures have been reported for landslides with varying geological structures and triggers. Linear depressions were widely observed in field images of toppling slopes in the Akaishi Mountains, Japan (Chigira and Kiho 1994). A linear depression, a steep step, and a low drainage density at the Chiu-fen-erh-shan landslide triggered by the 1999 Chi-Chi earthquake were detected through aerial photos taken 1 year before the collapse (Wang et al. 2003). A V-shaped scarplet at the Tsaoling landslide triggered by the 1999 Chi-Chi earthquake was also recognized on aerial photographs taken before the landslide. It was formed due to slope movement before the 1999 landslide (Chigira et al. 2003). Chigira et al. (2010) identified a 2-km-long ridge-top linear depression at the largest landslide triggered by the 2008 Wenchuan earthquake from the ORS images taken before the earthquake. Investigations of many deep-seated catastrophic landslides in Japan, induced by the heavy rainfall associated with two typhoon events, suggested that these landslides had been preceded by gravitational slope deformation (Chigira 2009; Chigira et al. 2013). Such slope deformation could be identified as small scarps or linear depressions along the crowns in aerial photographs before the landslides (Chigira et al. 2013). Numerous sackung features (shallow troughs and tension cracks) were found preceding the Aresawa rockslide triggered by snow melting, and new tension cracks emerging about 25 m behind the headscarp can be identified on ORS images taken at least 7 months before the collapse (Nishii et al. 2013).

The temporal behavior of DSGSDs has been studied within the last two decades owing to progress in geochronology, remote sensing, and instrumental monitoring (Pánek and Klimeš 2016), among which remote sensing techniques have played a critical role. Different remote sensing techniques have been applied to explore slope deformation history prior to failure, including light detection and ranging (LiDAR) (Carter et al. 2001; Haugerud et al. 2003; Chigira et al. 2004; Jaboyedoff et al. 2012; Kromer et al. 2015), synthetic aperture radar (SAR) (Wasowski and Bovenga 2014; Intrieri et al. 2018; Carlà et al. 2019; Chen et al. 2020), optical remote sensing (ORS) (Wang et al. 2003; Hervás et al. 2003; Nishii et al. 2013; Qi et al. 2021), or their combinations (Chigira et al. 2013; Casagli et al. 2016; Fan et al. 2017; Piroton et al. 2020). LiDAR provides high-resolution and three-dimensional point clouds of topography, which can be applied to landslide mapping (Jaboyedoff et al. 2008) and monitoring (Teza et al. 2007; Jaboyedoff et al. 2009; Kromer et al. 2015). However, LiDAR technique and high-quality topographic data have not yet been broadly available in many parts of the world. Time series analysis using SAR data allows for remote detection and characterization of ground surface displacements with sub-centimeter in precision and accuracy and tens of meters in spatial resolution (Bürgmann et al. 2000), making it particularly suitable

for the study of active slow-moving landslides (Cohen-Waeber et al. 2018). However, vegetation and large displacements often lead to incoherence in SAR images (Wasowski and Bovenga 2014). Multi-temporal ORS images have been widely used in landslide mapping (Lee 2005) and monitoring (Delacourt et al. 2007).

Given that the combined use of optical remote-sensing and in situ survey will still be the primary method for landslide early detection in the near future, this work attempts to extract reliable geomorphological precursors to rockslides visible on ORS images. For this purpose, five large rockslides in China were selected as illustrative examples. Multi-temporal satellite and UAV images were collected and interpreted manually to examine the potential geomorphological precursors to rockslides (e.g., cracks/scarps and rockfalls) and their temporal variations. Topographical, geological, and pre-sliding deformation data from different resources were collected to investigate the factors influencing existence and temporal behaviors of geomorphological precursors to large rockslides. Then, the implications of the proposed geomorphological precursors to rockslides for landslide early detection and warning were discussed, and the main findings were summarized.

Data and methods

Data

To study the geomorphological precursors to large rockslides, we selected and examined five large rockslides in China, including the 2014 Xiaoba, 2016 Su, 2017 Xinmo, 2017 Pusa, and 2018 Baige landslides (see Fig. 1 and Table 1). These landslides were developed in diverse landscapes shaped by different mountain formation mechanisms. The Su landslide (labeled No. 2 in Fig. 1) was initiated from a slope belonging to low mountains (Ouyang et al. 2018). The Xiaoba and Pusa landslides (labeled No. 1 and No. 4 in Fig. 1, respectively) were developed on slopes of medium mountains (Xing et al. 2016; Fan et al. 2019). The Xinmo and Baige landslides (labeled No. 3 and No. 5 in Fig. 1, respectively) were developed on slopes of high mountains (Fan et al. 2017; Xu et al. 2018). The diversity of landscape types of the selected landslides increases the confidence in using the proposed geomorphological precursors discussed in this study.

Geomorphological analysis

Multi-temporal optical remote sensing images were used for examining potential geomorphological precursors to large rockslides. The visual interpretation was conducted, and special attention was paid to geomorphological features visible on ORS images, such as large cracks, scarps, and rockfalls. The geometries of cracks/scarps and rockfalls were measured on multi-temporal ORS images to quantify their temporal evolutions. The landslide area interpreted from the post-sliding remote-sensing image defined the interpretation range of each ORS image. Following the same criteria, available high-resolution ORS images were collected and analyzed to track the potential precursors' earliest appearance time and

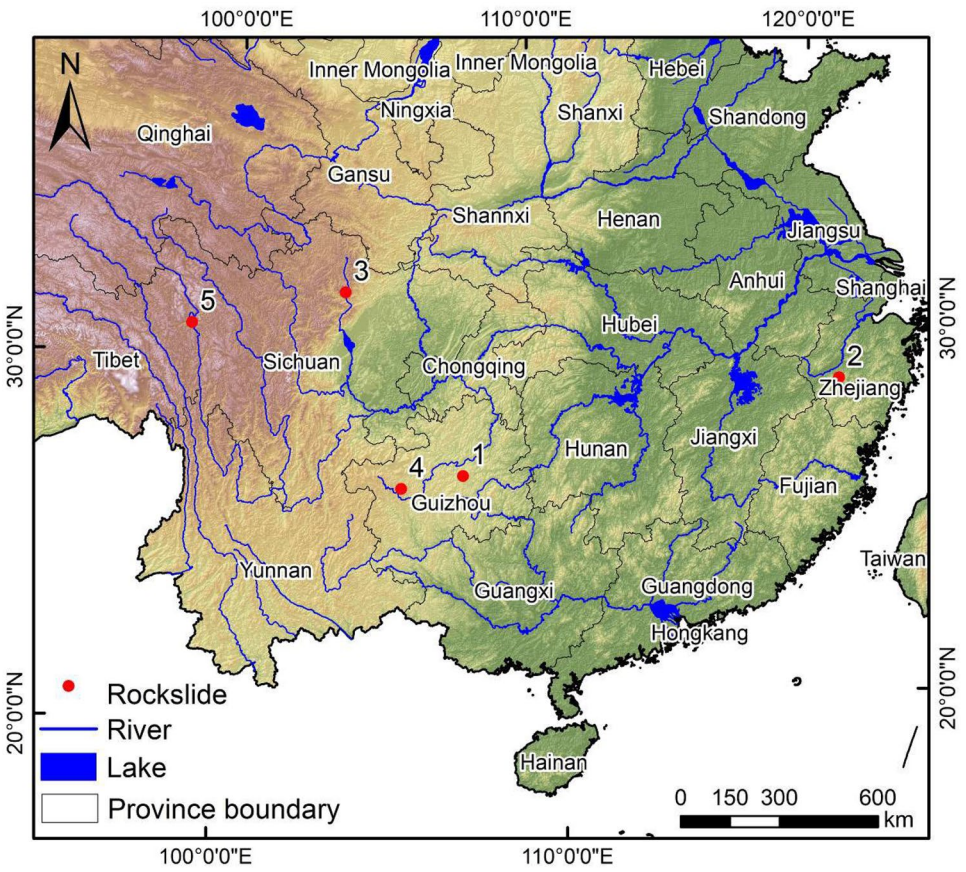

Fig. 1 Location map of the selected five large rockslides in China: (**1**) Xiaoba, (**2**) Su, (**3**) Xinmo, (**4**) Pusa, and (**5**) Baige landslides. The administration boundary data, river data, and SRTM (1 km) data were downloaded from the Resource and Environment Data Cloud Platform of the Institute of Geographic Science and Natural Resources Research, Chinese Academy of Sciences (https://www.resdc.cn/data.aspx)

Table 1 Summary of remote-sensing images

Landslide	Image data source	Taken date	Resolution (m)
Xiaoba	UAV	2011.07.01	0.2
	Pleiades	2013.08.28	0.5
	KOMPSAT	2014.01.22	1.0
	Gaofen-1	2014.07.23	2.0
	UAV	2014.08.27	0.2
Su	KeyHole	2000.07.01	2.0
	Quickbird	2010.12.20	0.61
	Quickbird	2013.10.13	0.61
	Unknown satellite	2015	1.0
	Planet	2016.03.02	3.0
	Planet	2016.08.18	3.0
	Planet	2016.09.26	3.0
	UAV	2016.09.29	0.2
Xinmo	Quickbird	2003.08.18	0.61
	Gaofen-2	2016.02.09	0.8
	Gaofen-2	2017.04.08	0.8
	UAV	2017.06.25	0.2
Pusa	Pleiades	2012.12.24	0.5
	Quickbird	2014.03.16	0.61
	Gaofen-2	2015.04.04	0.8
	Gaofen-1	2016.08.24	2.0
	Planet	2017.04.13	3.0
	Planet	2017.07.27	3.0
	Planet	2017.08.06	3.0
	Planet	2017.08.26	3.0
	UAV	2017.08.30	0.2
Baige	KeyHole	1966.02.08	2.0
	GeoEye-1	2011.03.04	0.41
	Ziyuan-3	2015.11.13	2.0
	Gaofen-2	2017.01.15	0.8
	Gaofen-2	2018.02.28	0.8
	Planet	2018.08.29	3.0
	UAV	2018.10.12	0.2

temporal evolution. The remote sensing images for each landslide are listed in Table 1, and the image interpretation results are described in "Geomorphological precursors to large rockslides."

Pre-sliding slope deformation

Available pre-sliding slope deformation data were extracted from the literature to study the relationship between geomorphological precursors and landslide kinematics. Currently, two types of slope deformation data are available for the selected five rockslides. In situ crown-crack monitoring data were used in the case of the Xiaoba landslide, whereas in the other four landslides, slope surface deformation data derived from SAR were used. The slope deformation data coverage varied from 243 to 1500 days before the failure, with an average of 791 days. These data were used to determine the creep stages defined by Intrieri et al. (2019): the first stage is a decelerating (primary) creep in which the strain rate decreases logarithmically; the second stage is a steady-state (secondary) creep in which creep occurs with a constant strain rate; the third stage is an accelerating (tertiary) creep involving an increasing strain rate, which leads to rupture.

Geomorphological precursors to large rockslides

Landslide geomorphological precursors and their temporal evolution

Multi-temporal ORS images were examined to determine whether any visible morphology can be identified as the geomorphological precursors to large rockslides. The results suggest that all the five landslides had cracks or scarps near their future crowns and rockfalls within the landslide source area before the slope failure. Furthermore, multi-temporal analyses of ORS images revealed that these geomorphological features were correlated with available slope deformation data. Hence, we suggest that cracks/scarps and rockfalls can be geomorphological precursors to large rockslides.

The cracks and scarps display as line features (i.e., with length much greater than width) in ORS images, and their plan shapes can be linear, concave, and convex, which are influenced by the local topography and geology. Cracks and scarps on the slope surface are usually associated with slope deformation and hint at landslide boundary. Chigira et al. (2013) defined one parameter called the scarp ratio to measure the relative size of scarps to the whole slopes. The scarp ratio is computed as the ratio of the horizontal scarp lengths to the horizontal slope length. The scarp ratios of the ten large landslides triggered by Typhoon Talas range from 5 to 21% based on the 1-m DEM obtained about 2 years before the slope failures (Chigira et al. 2013). Unfortunately, we did not have high-resolution DEMs for the five rockslides to quantify the scarp ratios. Hence, we decided to use the presence of cracks or scarps as geomorphological precursors to large rockslides.

In ORS images, rockfalls within the landslide source area are displayed as area features (i.e., polygons). Rockfalls within the landslide source area indicate severe rock damage before the slope failure, frequently observed for small to large rockslides (e.g., Paronuzzi and Bolla 2015; Kromer et al. 2015; Zhang et al. 2018). Our multi-temporal analyses suggest the rockfall activity within the landslide source area will be enhanced when the slope deformation is accelerated. This assertion is especially true for the landslides on the anti-dip slopes (e.g., Pusa and Baige landslides) and the igneous rock slope (e.g., Su landslide). To quantitatively track the temporal variations of rockfalls within the landslide source area, we defined a new parameter called

the rockfall area ratio (defined as the ratio of the cumulative rockfall area within the landslide source area over the total landslide source area). The rockfall area ratio can be considered a proxy measure of rock mass damage within the sliding mass. The rockfall area ratio and the associated temporal changes for the five selected rockslides were computed based on multi-temporal ORS analyses (see Table 2).

The geomorphological precursors to the five rockslides can be identified in ORS images taken several years or decades before the slope failure. According to the visual interpretations of the available ORS images, the Xiaoba, Xinmo, Pusa, Baige, and Su landslides had shown geomorphological precursors to landslides in ORS images taken at least 3, 14, 5, 52, and 16 years before the slope failures, respectively. Slope deformation data indicates that the two landslides at dip slopes (i.e., Xiaoba and Xinmo landslides) had episodic deformation and creep deformation before the slope failures. The largest landslide among the five examined landslides (i.e., the Baige landslide) is dominated by creep deformation and displays two creep stages (i.e., steady-state and accelerating creep). The Pusa and Su landslides have relatively short coverage of deformation data (less than 2 years) and show less reliable information about the slope deformation mechanisms and stages. The following sections describe the essential characteristics, deformation histories, and geomorphological precursors for each selected rockslide separately, and their key characteristics are summarized in Table 2.

The Xiaoba landslide

The Xiaoba landslide occurred at about 20:30 (GMT + 8) on August 27, 2014, in Daoping Town, Fuquan City, Guizhou Province. The Xiaoba rockslide developed on a dip slope with an attitude of strata being N20°E/SE∠46°, and the landslide volume was about 1.41×10^6 m^3 (Xing et al. 2016). An apparent "V" shape crack can be observed at the crown of the Xiaoba landslide in the 2011 image (Fig. 2d). The crown crack was ~ 27.0 m long and ~ 1.0 m wide. According to Fig. 2 b and e, the crown crack width increased to about 2.0 m by 2013, while its length showed no significant change. The post-sliding UAV image showed that this crack matched well with the future crown of the Xiaoba landslide (see Fig. 2f). The crack deformation was measured by local villagers using rulers between August 15, 2012, and August 25, 2014, within 1 to 15 days (Lin et al. 2018). The slope monitoring data suggests that the slope had a steady-state creep deformation at least 743 days before slope failure. The slope accelerated its deformation 243 days before the slope failure and had a cumulative displacement of about 8 m before the rapid collapse (Fig. 3). Rockfall activities were concentrated in the low section of the landslide source area (near the slope toe) and intensified before the slope failure. The rockfall area ratios interpreted from 2011, 2013, and 2014 (two) images were 0.195, 0.297, 0.321, and 0.335, respectively (see Table 2).

The Xinmo landslide

The Xinmo landslide occurred at about 6:00 (GMT + 8) on June 24, 2017, in Xinmo Village, Diexi Town, Mao County, Sichuan Province. The Xinmo landslide developed on a dip slope with an attitude of strata being N80°W/SW∠47°, and the landslide volume was about 4.3×10^6 m^3 (Fan et al. 2017). The 2003 image shows three cracks within the source area of the Xinmo landslide (see C1 ~ C3 in Fig. 4a). The strikes of the three cracks were perpendicular to the trend of the ridgeline (i.e., the cracks were stretched along the sliding direction). The cracks C1 and C3 developed into the west and east boundary of the failure mass, respectively (Fig. 4b). While the cracks of the Xinmo landslide showed no significant changes based on the 2003 and 2017 images, the rockfall area ratios were 0.343, 0.361, and 0.382 in 2003, 2016, and 2017, respectively, which implies the rockfall activities within the landslide source area were slightly enhanced during this period. Intrieri et al. (2018) presented the pre-sliding slope deformation data (Fig. 5) derived from the InSAR analysis using 45 phases of Sentinel-1 satellite images taken between October 9, 2014, and June 19, 2017. Figure 5 shows that the Xinmo landslide had episodic deformation and creep deformation before the slope failure. The slope deformation at the Xinmo landslide appeared to accelerate 275 days before the slope failure (Fig. 5).

The Pusa landslide

The Pusa landslide occurred at 10:30 (GMT + 8) on August 28, 2017, in Zhangjiawan Town, Nayong County, Guizhou Province, China. The Pusa landslide developed on an anti-dip slope (or a scarp slope) with an attitude of the strata was N80°E/SE∠5° ~ 10°, and the landslide volume was about 0.82×10^6 m^3 (Fan et al. 2019). The 2012 image shows two cracks (C1 and C2 cracks in Fig. 6a) parallel to the slope ridge line but on the other side of the mountain (i.e., backslope). The length of C1 and C2 cracks were 120 m and 160 m, respectively. A small rockfall deposit can be observed near the toe of the slope. In 2014, there were no significant changes in the lengths of C1 and C2 cracks, while a 25 m long crack (C3) developed between previous cracks (Fig. 6b). In 2015, no noticeable change was found in the cracks, but a new rockfall was observed near the northeastern boundary of the Pusa landslide (Fig. 6c). The unstable rock mass eventually slipped along a failure plane that outcropped as the longest crack (i.e., C2) (Fig. 6d). Chen et al. (2020) presented the pre-sliding slope deformation data of the Pusa landslide derived from the SAR analysis using the ALOS/PALSAR-2 and Sentinel-1A/B SAR imagery data (see Fig. 7). The slope deformation data suggest that the slope deformation accelerated ~ 144 days before the rapid landslide. The temporal variations of the rockfall area ratios are consistent with the pre-sliding slope deformation derived from the SAR analysis at the Pusa landslide (see Fig. 7). The rockfall area ratio rapidly rose from 0.4 to 0.9. The slope deformation increased by 0.13 m within three months before the Pusa landslide (see Fig. 7). These observations suggest a significant enhancement of slope deformation and rock damage in this period.

The Baige landslide

The Baige landslide occurred at 22:05 (GMT + 8) on October 10, 2018, on the right-side bank of the Jinsha River, and dammed the river in Baige Village, Boluo Town, Jiangda County, Xizang Autonomous Region. The Baige landslide developed on an anti-dip slope with an attitude of S35°E/SW∠40°, and the landslide volume was about 23×10^6 m^3 (Xu et al. 2018). Rockfalls were seen as a good indicator of slope instability at the Baige landslide. They appeared in the lower part of the source area (near the toe of the slope) as early as 1966 (Fig. 8a). A headscarp and rockfalls below the headscarp appeared

Table 2 Characteristics of the five selected large rockslides

	Landslide name	Xiaoba	Xinmo	Pusa	Baige	Su
Location and date	Sliding date	2014.08.27	2017.06.24	2017.08.28	2018.10.11	2016.09.28
	Latitude (° N)	26.958	32.080	26.635	31.082	28.784
	Longitude (° E)	107.361	103.663	105.449	98.705	119.304
Size	Area (10^6 m^2)	0.21	1.53	0.25	1.35	0.20
	Volume (10^6 m^3)	1.41	13.00	0.82	23.00	0.90
Mobility	Height difference (m)	250	1120	270	880	460
	Travel length (m)	810	2500	780	1900	1000
	Apparent friction angle (°)	17.2	24.1	19.1	24.9	24.7
Geology	Formation	Doushantuo (Z1ds)	Zagunao (T2z)	Yelang (T_1y)	Xiongsong (Ptxna)	Cretaceous (γ 53)
	Lithology	Dolomite	Sandstone, slate, phyllite	Limestone	Gneiss, ophiolite	Granite
	Slope structure	Dip	Dip	Anti-dip	Anti-dip	NA
	Dip angle (°)	46	47	5 ~ 10	40	NA
Landslide source area	Pre-sliding slope (°)	24	50	61	29	22
	Post-sliding slope (°)	37	45	43	37	50
	Height difference (m)	170	280	270	580	160
	Length (m)	368	510	170	1200	160
	Width (m)	180	380	330	500	220
	Thickness (m)	19	72	18	43	30
	Area (10^6m^2)	0.074	0.182	0.045	0.540	0.030
Pre-sliding optical remote sensing analysis	Year-Rockfall area ratio	2011–0.195, 2013–0.297, 2014–0.321, 2014–0.335	2003–0.343, 2016–0.361, 2017–0.382	2012–0.184, 2014–0.184, 2015–0.369, 2016–0.369, 2017–0.387, 2017–0.899, 2017–0.923, 2017–0.923	1966–0.033, 2011–0.397, 2015–0.423, 2017–0.441, 2018–0.557, 2018–0.644	2000–0.048, 2010–0.315, 2013–0.482, 2015–0.668, 2016–0.691, 2016–0.693, 2016–0.771
Pre-sliding slope deformation analysis	Data source	In situ	SAR	SAR	SAR	SAR
	Displacement data coverage (days) *	735	990	243	1500	488
	Accelerating period (days) **	243	275	144	507	NA

*The duration of available pre-sliding slope deformation data derived from SAR analysis or in-situ monitoring

**The duration of slope accelerating creep deformation

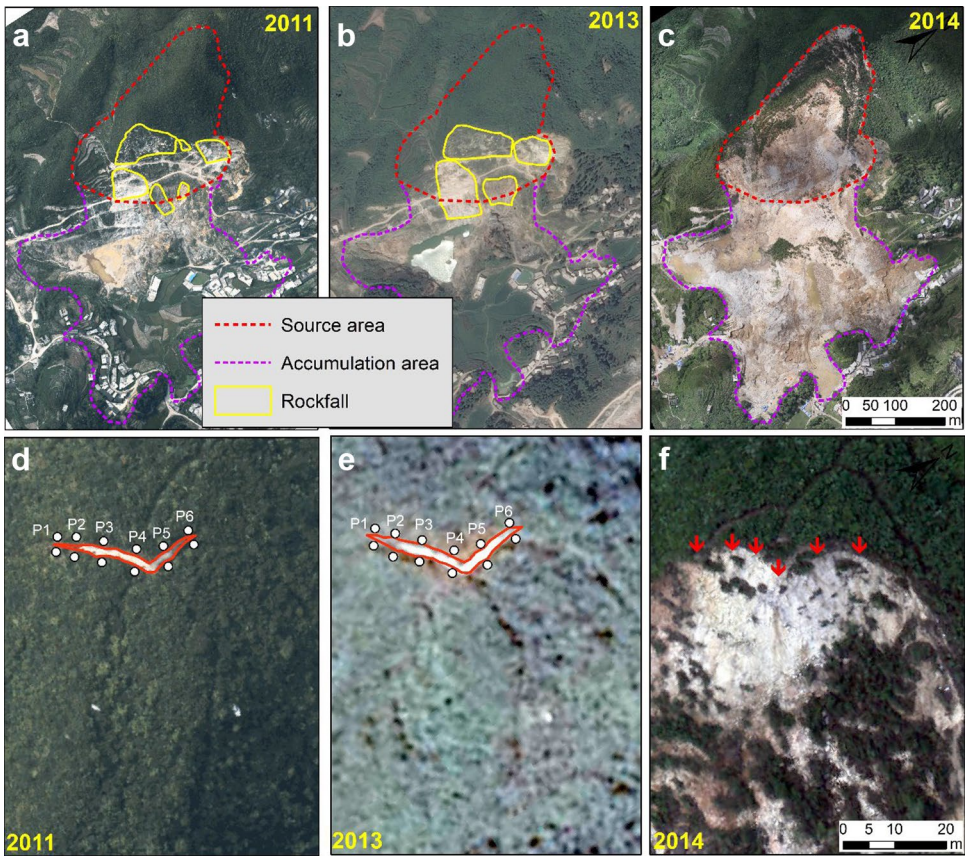

Fig. 2 Slope deformation characteristics at the Xiaoba landslide visible on different ORS images. **a** UAV image taken on July 1, 2011. **b** Pleiades satellite image taken on August 28, 2013. **c** UAV image taken on August 27, 2014. **d**–**f** Close views of **a**–**c**, respectively. Red arrows in **f** indicate the upper boundary of cracks in **d** and **e**

in the 2011 image, and the sizes of rockfalls in the downslope part of the landslide were enhanced significantly (Fig. 8b). The rockfall in the downslope portion of the landslide was slightly enlarged in the 2015 and 2017 images (Fig. 8c, d). The Gaofen-2 image taken on February 28, 2018, shows significant slope deformation as the rockfall activities at the downslope part and near the headscarp are enhanced (Fig. 8e). In the image taken on August 29, 2018, rockfalls are dominant in the landslide source area (Fig. 8f), indicating the slope was close to the final failure (Xu et al. 2018). The rockfall area ratios changed from 0.03 in 1966 to 0.64 in 2018 (42 days before the slope failure). SAR pixel offset tracking (Li et al. 2020) was used to investigate the pre-sliding slope deformation of the Baige landslide between October 2014 and October 2018. The results suggest that the steady-state and the accelerating creep stages were delimited by March 2017 (i.e., 507 days before the failure) (Fig. 9). The average deformation rate of the Baige landslide during the steady-state creep was 0.02 m/day (i.e., 7.3 m/year), and the slope had an accumulative displacement of 60 m before the slope failure. Although rockfall area ratio data are scarce due to the large temporal interval of selected ORS images, there is a clear trend that the rockfall area ratio increased significantly during the accelerating creep stage (Fig. 9). This finding suggests a strong correlation between rockfall activity and slope deformation, supporting the use of rockfalls as geomorphological precursors to large rockslides.

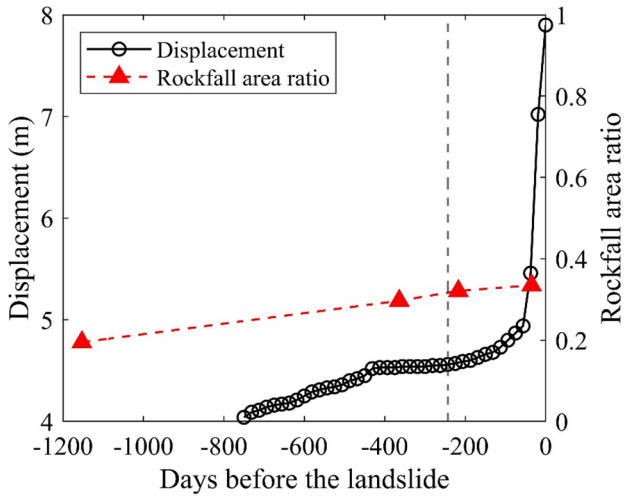

Fig. 3 Deformation and rockfall area time histories of the Xiaoba landslide. Displacement data are the averaged displacements at P1 ~ 6 in Fig. 2d measured at irregular frequency (Lin et al. 2018). The dashed gray line indicates the approximate start of accelerating creep

The Su landslide

The Su landslide occurred at 17:28 (GMT + 8) on September 28, 2016, in the Su Village, Beijie Town, Suichang County, Lishui City, Zhejiang Province, eastern China. The Su landslide was developed on a slope

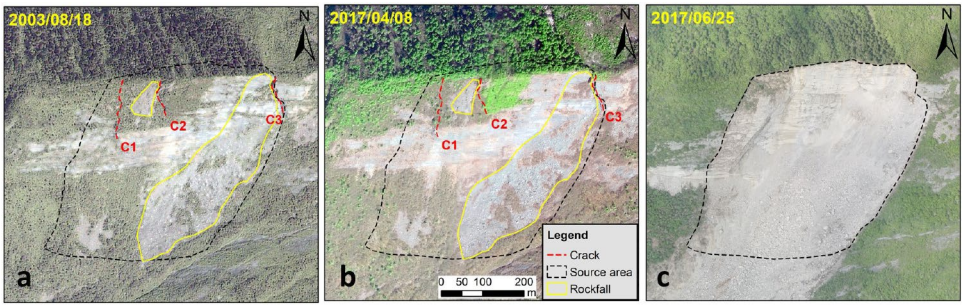

Fig. 4 Slope deformation characteristics at the Xinmo landslide visible on different ORS images. **a** Quickbird satellite image taken on August 18, 2003. **b** Gaofen-2 image taken on April 8, 2017. **c** UAV image taken on June 25, 2017

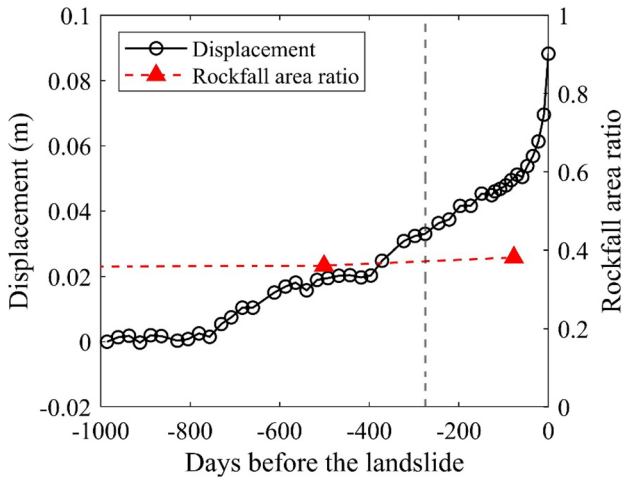

Fig. 5 Deformation and rockfall area time histories of the Xinmo landslide. The displacement data are from Intrieri et al. (2018). The dashed gray line indicates the start time of accelerating creep

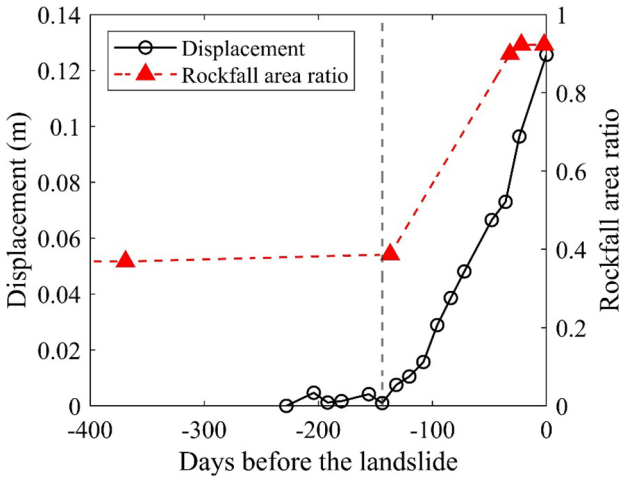

Fig. 7 Deformation and rockfall area time histories of the Pusa landslide. The displacement data are obtained by SAR analysis (Chen et al. 2020). The dashed gray line indicates the approximate start of accelerating creep

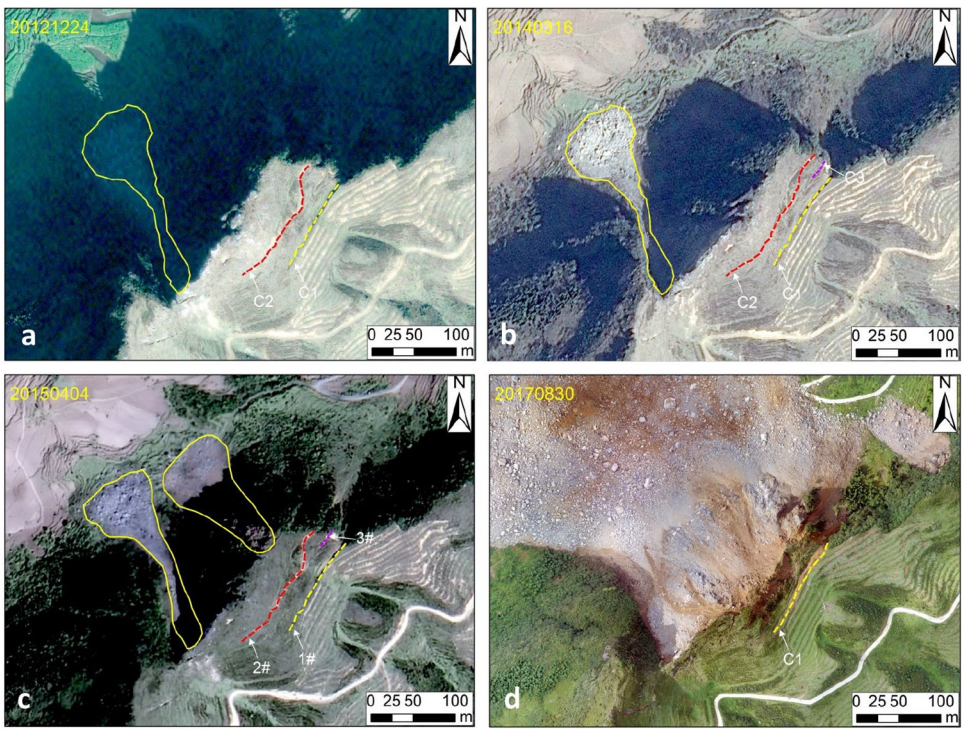

Fig. 6 Slope deformation characteristics at the Pusa landslide visible on different ORS images. **a** Pleiades satellite image taken on December 24, 2012. **b** Quickbird satellite image taken on March 16, 2014. **c** Gaofen-2 image taken on April 4, 2015. **d** UAV image taken on August 30, 2017

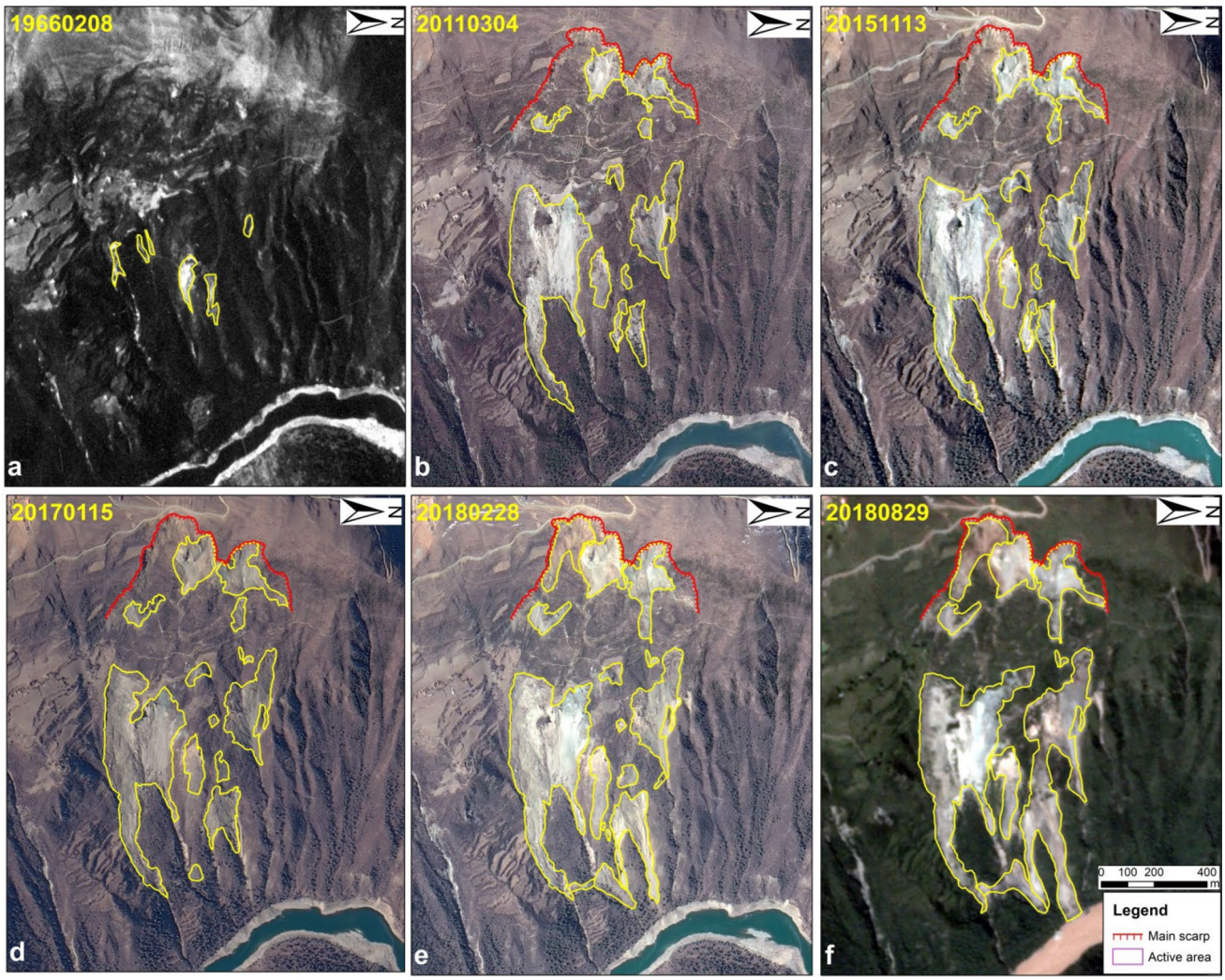

Fig. 8 Slope deformation characteristics at the Baige landslide visible on different ORS images. **a** KeyHole satellite image taken on February 8, 1996. **b** GeoEye-1 satellite image taken on March 4, 2011. **c** Ziyuan-3 image taken on November 13, 2015. **d** Gaofen-2 satellite image taken on January 15, 2017. **e** Gaofen-2 image taken on February 28, 2018. **f** Planet image taken on August 29, 2018

mainly consisting of monzonitic granite, and the landslide volume was estimated as 0.9×10^6 m^3 (Ouyang et al. 2018). Distinct deformation characteristics such as scarps and rockfalls were identified on ORS images (taken as early as 2000) (Fig. 10a). According to the 2010 and 2013 images, there was no significant extension of the scarp, but the rockfall range and size increased during that period (Fig. 10b, c). The 2015 image shows that the crown crack had extended to the east and west boundaries of the landslide source area, and the rockfall area was slightly increased during this period (Fig. 10d). The extended crown crack displayed on the 2015 image controls the 2016 sliding event as it is identical to the rear boundary of the Su landslide. The rockfall area ratio increased from 0.05 in 2000 to 0.77 in 2016. The SAR analysis using Persistent Scatterer Interferometry (PSI) conducted by Ouyang et al. (2019) suggests the source area of the Su landslide showed linear deformation starting no later than April 25, 2015. The average deformation rate was about 0.1 m/year, and the cumulative displacement was 0.15 m during this period. The deformation rate remained linear until the rapid failure triggered by the intense rain associated with Typhoon Catfish (Ouyang et al. 2018). Accelerating deformation induced by this short-term intensive triggering force was not captured by the SAR analysis, and the start time of the accelerating creep stage is not available (Fig. 11).

Influential factors on landslide geomorphological precursors

As geomorphological precursors to rockslides are associated with gravitational slope deformation, they may be influenced by internal factors (e.g., slope geometry, geological structure, and deformation mechanism) and external trigger forces (e.g., heavy rainfall, human disturbance, and earthquake). This section investigates the potential factors affecting existence and temporal evolution of geomorphological precursors to rockslides. Although cracks or scarps are recognized on the pre-sliding ORS images at the five landslides, they show different image characteristics and roles in constraining the landslide source area. The Xinmo and Pusa landslides were initiated from steep crest sections of thin mountain ridges (with an average

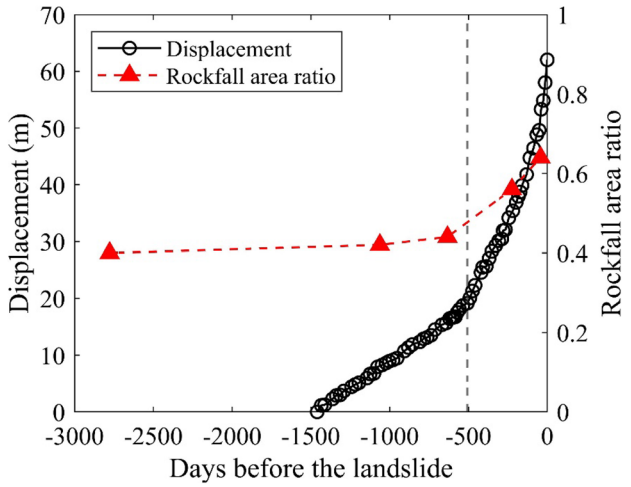

Fig. 9 Deformation and rockfall area time histories of the Baige landslide. The displacement data are from the SAR analysis by Li et al. (2020). The dashed gray line indicates the approximate start of accelerating creep

slope of 50° and 61°, respectively). They displayed small cracks only identifiable with high-resolution images and careful interpretation. On the other hand, the Xiaoba, Baige, and Su landslides were developed at the downslope sections with less steep topographic gradients (with an average slope of 24°, 29°, and 22°, respectively) and had shown relatively large scarps near the future landslide crowns. Besides, the cracks at the Xinmo landslide controlled the side boundaries of the future landslide and were perpendicular to the landslide's rear boundary (as well as the ridgeline). The cracks at the Pusa landslide controlled its rear boundary, and the two sides of the sliding mass were near the natural slope irregularities (see Fig. 6). These findings suggest that the local topography influences the type of geomorphological precursors to rockslides (cracks or scarps) and their spatial location. Rockslides initiated from steep and thin crest sections of mountain ridges can have tensile cracks near future landslides' rear or side boundary. On the other hand, rockslides developed within gentle and thick downslope sections tend to have scarps near future landslide crowns.

The rockfalls within the landslide source area tend to locate at "key blocks" where slope mass provides forces resisting sliding.

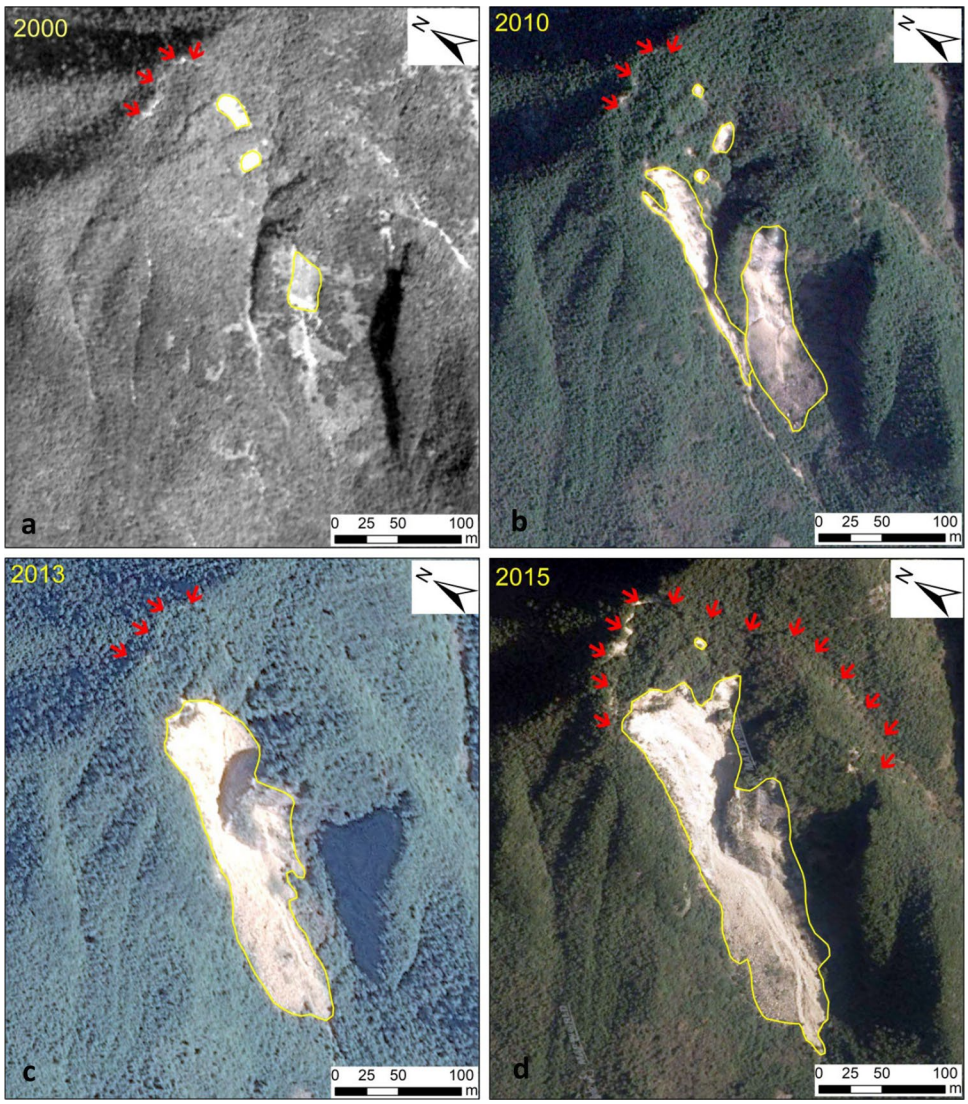

Fig. 10 Slope deformation characteristics at the Su landslide visible on different ORS images. **a** KeyHole satellite image taken on an unknown date in 2000. **b** Quickbird satellite image taken on December 20, 2010. **c** Quickbird satellite image taken on October 13, 2013. **d** Tiandi map image taken on an unknown date in 2015

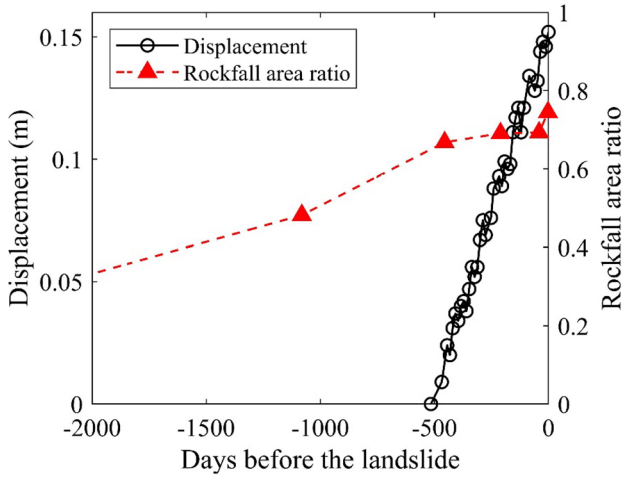

Fig. 11 Deformation and rockfall area time histories of the Su landslide. The displacement data are from Ouyang et al. (2019)

Rockfalls were mainly distributed within the downslope section at the Xiaoba, Baige, and Su landslides. At the Xinmo and Pusa landslides, rockfalls were located near the future side boundaries. Rockfall activities within the landslide source area could interplay with slope deformation. On the one hand, slope deformation can cause rock damage and rockfalls within the landslide source area, especially where the rock mass plays the role of a key block (Qin et al. 2020). For example, the rockfalls at the Xinmo landslides were from key blocks that prevent the sliding mass from detaching from the crest (see Fig. 4). On the other hand, the rockfalls within the landslide source area can further deteriorate the slope stability as they affect the rock strength and groundwater infiltration. The spatial locations of rockfalls could be used together with cracks/scarps to detect landslides and constrain the potential landslide boundary before slope failure.

Generally, cracks or scarps show less significant temporal variations than rockfalls within the landslide source area at the five rockslides. Figure 12 shows the temporal changes of rockfall area ratios and displacement ratios (defined as the ratio of cumulative slope displacement to the maximum cumulative slope displacement before the slope failure) of these landslides. The rockfall area ratio shows unique temporal variation at the Xinmo landslide compared to the other four landslides. The rockfall activity within the landslide source area at the Xinmo landslide seemed to remain unchanged before the slope failure, while those at the other four landslides were strongly enhanced (Fig. 12b). It appears that geological structure affects rockfall activity within the landslide source area. The landslides developed on anti-dip and igneous rock slopes show a more significant rise in rockfall area ratio before the slope failure than the landslides on dip slopes (Fig. 12b). The landslides developed on anti-dip and igneous rock slopes have a rockfall area ratio larger than 0.6, implying widespread rock damage on these anti-dip and igneous rock slopes before slope failures. The Pusa landslide has a rockfall area ratio of up to 0.92 in the latest pre-sliding image, which suggests that the slope might have been in critical condition just before the catastrophic failure. The rockfall activities were not severe within the landslide source areas of the two landslides developed on dip slopes and did not show an accelerated trend with time. Nevertheless, these two rockslides developed on dip slopes had rockfall area ratios larger than 0.3 before their catastrophic failures.

The accelerating period, indicating the approximate duration of the final accelerating creep stage before the slope failure, was derived from the time series analysis of pre-sliding slope deformation data. The accelerating periods of the four landslides (excluding the Su landslide as its start time of accelerating creep was not identified) were computed in Table 2 and shown in Fig. 13. The four landslides have an accelerating period ranging from 144 days (at the Pusa landslide) to 507 days (at the Baige landslide), with an average of 292 days. The accelerating period seems to have a strong positive correlation with the landslide size (by landslide volume), and the best-fit linear regression model has a coefficient of determination (R^2) of 0.86 (Fig. 13). It is noted that the mining activities at the Xiaoba and Pusa landslides may cause irregular episodic deformation and influence the accelerating periods before slope failures. Future studies to collect

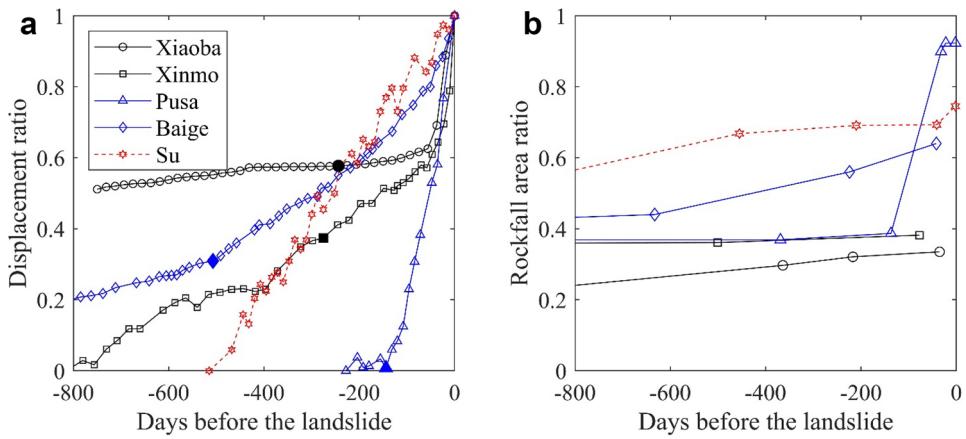

Fig. 12 Temporal variations of **a** displacement ratio (the cumulative slope displacement over the maximum cumulative displacement) and **b** rockfall area ratio (the cumulative rockfall area over the landslide source area) within the 800 days before slope failures of the five selected rockslides. The black, blue, and red lines are for landslides developed within dip, anti-dip, and igneous rock slopes. The solid markers in **a** indicate the start time of the accelerating creep stage, which is available for landslides except for the Su landslide

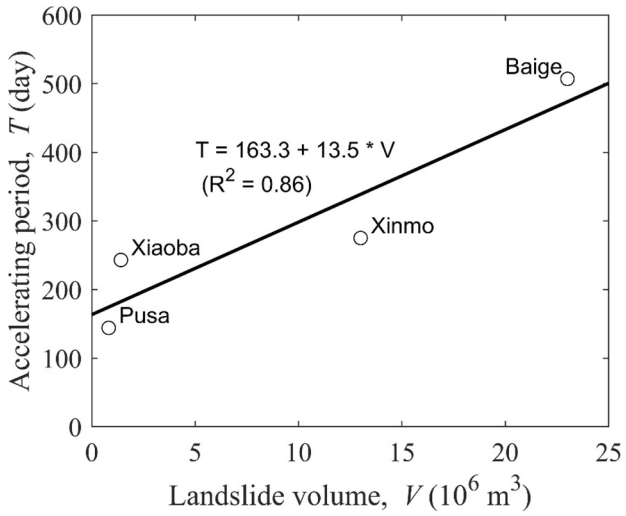

Fig. 13 Correlation between accelerating period of slope deformation and landslide volume. The Su landslide is excluded because its start time of accelerating creep deformation is not available

more case histories to improve the correlation shown in Fig. 13 are warranted.

Conclusions

This study examined geomorphological precursors to large rockslides visible on ORS images using multi-temporal data analyses. Five rockslides developed on dip (i.e., Xiaoba and Xinmo landslides), anti-dip (i.e., Pusa and Baige landslides), and igneous rock slopes (i.e., Su landslide) were selected as illustrative cases. In addition, topographical, geological, and pre-sliding deformation data were collected to investigate the correlation between slope deformation and geomorphological precursors and their influential factors. The main findings from this study include:

1. Two geomorphological features, cracks/scarps and rockfalls, are considered precursors to large rockslides. They can be identified from ORS images taken at least 3 to 52 years before the slope failure at the five landslides.
2. Local topography can affect the line-type geomorphological precursors to rockslides (i.e., cracks or scarps) and their spatial location. For example, rockslides initiated from steep and thin crests can have tensile cracks near the rear or side boundary of future landslides. However, rockslides initiated from gentle and thick downslope tend to have scarps near the future landslide crowns.
3. Rockfalls within the landslide source area tend to locate at "key blocks" where slope mass provides forces resisting sliding. In the case of the Xiaoba, Baige, and Su landslides, rockfalls were mainly distributed within the downslope. In the case of the Xinmo and Pusa landslides, they were located near the side boundaries of the sliding block.
4. The rockfall area ratio is correlated with landslide deformation stages inferred by pre-sliding slope deformation data. The rockfall area ratio ranged from 0.33 to 0.92 before the catastrophic slope failures at the five landslides. The landslides developed on anti-dip and igneous rock slopes show a more significant rise of rockfall area ratio before the slope failure than the landslides on dip slopes.
5. Accelerating period seems to have a strong positive correlation with the landslide volume, and the best-fit linear regression model has a coefficient of determination (R^2) of 0.86.

As a final remark, this article has shown that cracks/scarps and rockfalls visible and measurable in ORS images can be used as geomorphological precursors to the five large rockslides. However, the findings may not extend to landslides elsewhere due to the limited number of case histories examined in this work and the complex effects of slope geometry, geological structure, and external forces on landslide kinematics. Further studies to collect more landslide case histories are warranted to validate the proposed geomorphological precursors to rockslides.

Acknowledgements

The authors would like to thank the editor and three anonymous reviewers for providing constructive comments that improved the quality of this article. The corresponding author would like to thank Professor C. Hsein Juang for giving valuable advice on writing.

Funding

This research is supported by the National Key Research and Development Program of China (Grant No. 2021YFC3000401), the National Key Research and the National Natural Science Foundation of China (Grant Nos. 41941019), and the Second Tibetan Plateau Scientific Expedition and Research Program (STEP) (Grant No. 2019QZKK0201).

Declarations

Conflict of interest The authors declare no competing interests.

References

Bürgmann R, Rosen PA, Fielding EJ (2000) Synthetic aperture radar interferometry to measure Earth's surface topography and its deformation. Annu Rev Earth Planet Sci 28(1):169–209

Carlà T, Intrieri E, Raspini F, Bardi F, Farina P, Ferretti A, Colombo D, Novali F, Casagli N (2019) Perspectives on the prediction of catastrophic slope failures from satellite InSAR. Sci Rep 9(1):1–9

Carter W, Shrestha R, Tuell G, Bloomquist D, Sartori M (2001) Airborne laser swath mapping shines new light on Earth's topography. Eos 82(46):549–555

Casagli N, Cigna F, Bianchini S, Hölbling D, Füreder P, Righini G, Del Conte S, Friedl B, Schneiderbauer S, Iasio C, Vlcko J (2016) Landslide mapping and monitoring by using radar and optical remote sensing: examples from the EC-FP7 project SAFER. Remote Sens Appl: Soc Environ 4:92–108

Chen L, Zhao C, Kang Y, Chen H, Yang C, Li B, Liu Y, Xing A (2020) Pre-event deformation and failure mechanism analysis of the Pusa landslide, China with multi-sensor SAR imagery. Remote Sens 12(5):856

Chigira M, Kiho K (1994) Deep-seated rockslide-avalanches preceded by mass rock creep of sedimentary rocks in the Akaishi Mountains, central Japan. Eng Geol 38(3–4):221–230

Chigira M, Wang W, Furuya T, Kamai T (2003) Geological causes and geomorphological precursors of the Tsaoling landslide triggered by the 1999 Chi-Chi earthquake. Taiwan Eng Geol 68(3–4):259–273

Chigira M, Duan F, Yagi H, Furuya T (2004) Using an airborne laser scanner for the identification of shallow landslides and susceptibility assessment in an area of ignimbrite overlain by permeable pyroclastics. Landslides 1(3):203–209
Chigira M (2009) September 2005 rain-induced catastrophic rockslides on slopes affected by deep-seated gravitational deformations, Kyushu, southern Japan. Eng Geol 108(1–2):1–15
Chigira M, Wu X, Inokuchi T, Wang G (2010) Landslides induced by the 2008 Wenchuan earthquake, Sichuan. China Geomorphology 118(3–4):225–238
Chigira M, Tsou CY, Matsushi Y, Hiraishi N, Matsuzawa M (2013) Topographic precursors and geological structures of deep-seated catastrophic landslides caused by Typhoon Talas. Geomorphology 201:479–493
Cohen-Waeber J, Bürgmann R, Chaussard E, Giannico C, Ferretti A (2018) Spatiotemporal patterns of precipitation-modulated landslide deformation from independent component analysis of InSAR time series. Geophys Res Lett 45(4):1878–1887
Delacourt C, Allemand P, Berthier E, Raucoules D, Casson B, Grandjean P, Pambrun C, Varel E (2007) Remote-sensing techniques for analysing landslide kinematics: a review. Bull Soc Geol Fr 178(2):89–100
Fan X, Xu Q, Scaringi G, Dai L, Li W, Dong X, Zhu X, Pei X, Dai K, Havenith HB (2017) Failure mechanism and kinematics of the deadly June 24, 2017 Xinmo landslide, Maoxian, Sichuan. China Landslides 14(6):2129–2146
Fan X, Xu Q, Scaringi G, Zheng G, Huang R, Dai L, Ju Y (2019) The "long" runout rock avalanche in Pusa, China, on August 28, 2017: a preliminary report. Landslides 16(1):139–154
Gong W, Juang CH, Wasowski J (2021) Geohazards and human settlements: Lessons learned from multiple relocation events in Badong. China-Engineering Geologist's Perspective Eng Geol 285:106051
Haugerud RA, Harding DJ, Johnson SY, Harless JL, Weaver CS, Sherrod BL (2003) High-resolution lidar topography of the Puget Lowland. Washington GSA Today 13(6):4–10
Hervás J, Barredo JI, Rosin PL, Pasuto A, Mantovani F, Silvano S (2003) Monitoring landslides from optical remotely sensed imagery: the case history of Tessina landslide. Italy Geomorphology 54(1–2):63–75
Huang R (2007) Large-scale landslides and their sliding mechanisms in China since the 20th century. Chin J Rock Mech Eng 26(31):433–454 (in Chinese with English abstract)
Huggel C (2009) Recent extreme slope failures in glacial environments: effects of thermal perturbation. Quat Sci Rev 28(11–12):1119–1130
Intrieri E, Raspini F, Fumagalli A, Lu P, Del Conte S, Farina P, Allievi J, Ferretti A, Casagli N (2018) The Maoxian landslide as seen from space: detecting precursors of failure with Sentinel-1 data. Landslides 15(1):123–133
Intrieri E, Carlà T, Gigli G (2019) Forecasting the time of failure of landslides at slope-scale: a literature review. Earth Sci Rev 193:333–349
Jaboyedoff M, Pedrazzini A, Horton P, Loye A, Surace I (2008) Preliminary slope mass movements susceptibility mapping using LIDAR DEM. In: Proceedings of 61st Canadian geotechnical conference, pp 419–426
Jaboyedoff M, Oppikofer T, Locat A, Locat J, Turmel D, Robitaille D, Demers D, Locat P (2009) Use of ground-based LIDAR for the analysis of retrogressive landslides in sensitive clay and of rotational landslides in river banks. Can Geotech J 46:1379–1390
Jaboyedoff M, Oppikofer T, Abellán A, Derron MH, Loye A, Metzger R, Pedrazzini A (2012) Use of LIDAR in landslide investigations: a review. Nat Hazards 61(1):5–28
Kromer RA, Hutchinson DJ, Lato MJ, Gauthier D, Edwards T (2015) Identifying rock slope failure precursors using LiDAR for transportation corridor hazard management. Eng Geol 195:93–103
Lee S (2005) Application of logistic regression model and its validation for landslide susceptibility mapping using GIS and remote sensing data. Int J of Remote Sens 26(7):1477–1491
Li M, Zhang L, Ding C, Li W, Luo H, Liao M, Xu Q (2020) Retrieval of historical surface displacements of the Baige landslide from time-series SAR observations for retrospective analysis of the collapse event. Remote Sens Environ 240:111695
Lin F, Wu LZ, Huang RQ, Zhang H (2018) Formation and characteristics of the Xiaoba landslide in Fuquan, Guizhou. China Landslides 15(4):669–681
Nishii R, Matsuoka N, Daimaru H, Yasuda M (2013) Precursors and triggers of an alpine rockslide in Japan: the 2004 partial collapse during a snow-melting period. Landslides 10(1):75–82
Ouyang C, Zhao W, Xu Q, Peng D, Li W, Wang D, Zhou S, Hou S (2018) Failure mechanisms and characteristics of the 2016 catastrophic rockslide at Su village, Lishui. China Landslides 15(7):1391–1400
Ouyang C, Zhao W, An H, Zhou S, Wang D, Xu Q, Li W, Peng D (2019) Early identification and dynamic processes of ridge-top rockslides: implications from the Su Village landslide in Suichang County, Zhejiang Province. China Landslides 16(4):799–813
Pánek T, Klimeš J (2016) Temporal behavior of deep-seated gravitational slope deformations: A review. Earth Sci Rev 156:14–38
Paronuzzi P, Bolla A (2015) Gravity-induced rock mass damage related to large en masse rockslides: evidence from Vajont. Geomorphology 234:28–53
Piroton V, Schlögel R, Barbier C, Havenith HB (2020) Monitoring the recent activity of landslides in the Mailuu-Suu Valley (Kyrgyzstan) using radar and optical remote sensing techniques. Geosci 10(5):164
Qi W, Yang W, He X, Xu C (2021) Detecting Chamoli landslide precursors in the southern Himalayas using remote sensing data. Landslides 18(10):3449–3456
Qin CA, Chen G, Zhu J, Tang P (2020) A precursor of bedding rockslide: rock spalling in the key block triggered by tensile cracks. Bull Eng Geol Environ 79(5):2513–2528
Teza G, Galgaro A, Zaltron N, Genevois R (2007) Terrestrial laser scanner to detect landslide displacement fields: a new approach. Int J Remote Sens 28(16):3425–3446
Wang WN, Chigira M, Furuya T (2003) Geological and geomorphological precursors of the Chiu-fen-erh-shan landslide triggered by the Chi-chi earthquake in central Taiwan. Eng Geol 69(1–2):1–13
Wasowski J, Bovenga F (2014) Investigating landslides and unstable slopes with satellite Multi-Temporal Interferometry: Current issues and future perspectives. Eng Geol 174:103–138
Xing A, Xu Q, Zhu Y, Zhu J, Jiang Y (2016) The August 27, 2014, rock avalanche and related impulse water waves in Fuquan, Guizhou. China Landslides 13(2):411–422
Xu Q, Zheng G, Li W, He C, Dong X, Guo C, Feng W (2018) Study on Successive Landslide Damming Events of Jinsha River in Baige Village of October 11 and November 3, 2018. J Eng Geol 26(6):1534–1551 (in Chinese with English abstract)
Zhang M, McSaveney M, Shao H, Zhang C (2018) The 2009 Jiweishan rock avalanche, Wulong, China: precursor conditions and factors leading to failure. Eng Geol 233:225–230

Weile Li · Weiwei Zhan (✉) · Huiyan Lu · Qiang Xu · Xiangjun Pei · Runqiu Huang
State Key Laboratory of Geohazard Prevention and Geoenvironment Protection, Chengdu University of Technology, Chengdu 610059, China
Email: weiwei.zhan@tufts.edu

Weiwei Zhan
Department of Civil and Environmental Engineering, Tufts University, Medford, MA 02155, USA
Email: weiwei.zhan@tufts.edu

Dong Wang
China Railway Eryuan Engineering Group Co. Ltd., Chengdu 610031, China

Daqing Ge
China Aero Geophysical Survey & Remote Sensing, Center for Land and Resources (AGRS), Beijing 100083, China